

## Development of an Active Aeroelastic Parametric Wing Apparatus

Schildkamp, R.R.M.; Wang, Xuerui; Chang, J.; De Breuker, R.; Sodja, J.

**Publication date**

2022

**Document Version**

Final published version

**Published in**

International Forum on Aeroelasticity and Structural Dynamics

**Citation (APA)**

Schildkamp, R. R. M., Wang, X., Chang, J., De Breuker, R., & Sodja, J. (2022). Development of an Active Aeroelastic Parametric Wing Apparatus. In *International Forum on Aeroelasticity and Structural Dynamics*

**Important note**

To cite this publication, please use the final published version (if applicable).  
Please check the document version above.

**Copyright**

Other than for strictly personal use, it is not permitted to download, forward or distribute the text or part of it, without the consent of the author(s) and/or copyright holder(s), unless the work is under an open content license such as Creative Commons.

**Takedown policy**

Please contact us and provide details if you believe this document breaches copyrights.  
We will remove access to the work immediately and investigate your claim.

## DEVELOPMENT OF AN ACTIVE AEROELASTIC PARAMETRIC WING APPARATUS

Roderick Schildkamp<sup>1</sup>, Xuerui Wang<sup>1</sup>, Jing Chang<sup>1</sup>, Roeland De Breuker<sup>1</sup>, Jurij Sodja<sup>1</sup>

<sup>1</sup>Delft University of Technology

Kluyverweg 1, 2629 HS Delft

R.R.M.Schildkamp@tudelft.nl, X.Wang-6@tudelft.nl J.Chang-2@tudelft.nl,

R.DeBreuker@tudelft.nl, J.Sodja@tudelft.nl

**Keywords:** aeroservoelasticity, wind tunnel, experimental, design, gust load alleviation, spoiler

**Abstract:** This paper presents the development and initial characterization of an active, parametric wing section with aileron and spoiler control surfaces. This wing section is intended to replace the currently used passive wing section setup and facilitate research in active control techniques of aeroelastic phenomena such as flutter, gust load alleviation, and limit cycle oscillations. Baseline capabilities of the passive setup such as a variable center of mass, pitch axis location and spring stiffnesses are retained, while control surfaces, sensors, a single-board computer, and a mechanism for adjustable aileron free play were included in the new design. Various system identification tests, such as a ground vibration test, flutter and control reversal speed tests, the actuator frequency response and static aerodynamic interaction between spoiler and aileron, were performed to identify the characteristics of the wing section. Finally, as a proof-of-concept, gust load alleviation tests show the difference between open- and closed-loop gust response when the aileron and spoiler are controlled with PID control.

### 1 INTRODUCTION

The use of composite materials and increasing the wing aspect ratio are two commonly used methods to lower aircraft emissions by reducing the weight and drag of the aircraft. These measures result in a more flexible structure, they also lead to increased susceptibility to gust and maneuver load increments, lower flutter speed and the occurrence of limit cycle oscillations. These problems can be mitigated using active control techniques [1].

Active aeroelastic control techniques have been demonstrated using a variety of control surfaces and control laws. Using a wing section with trailing edge flap and a linear quadratic Gaussian controller, Viperman et al. manage to extend the flutter boundary by 12% as well as implement gust load alleviation (GLA) [2]. GLA using linear quadratic regulator (LQR) and model predictive control (MPC) on a low-cost, half-span aircraft model is shown by Barzgaran et al. A comparison of both methods showed a load reduction of 40% using MPC, whereas LQR only achieved a 12% reduction in load [3]. Cassero et al. demonstrate flutter suppression using a wing section model with leading edge spoilers, first using PID control [4] and later using model reference adaptive control (MRAC) [5]. Another example of aeroelastic control is given by Lancelot and De Breuker, using a passively actuated spoiler for GLA to obtain a 9% load reduction [6]. Besides the conventional aileron and spoiler, aeroelastic control using more unconventional control surfaces also exist. Examples include using morphing wings for

both gust and maneuver load alleviation [7, 8]. A final example of unconventional control surfaces for aeroelastic control is the flapping wingtip, achieving a peak load reduction in excess of 90% [9].

Current facilities at Delft University of Technology allow for research on the previously mentioned aeroelastic phenomena. These facilities include a gust generator [10] and a parametric aeroelastic apparatus which houses a passive wing section [11]. Research in active control techniques however requires a new wing section with at least one control surface. The purpose of this study is therefore to develop an active wing section to both enable future research in active control techniques and to study the interaction between aileron and spoiler for varying properties of the aeroelastic system.

This paper presents the design, development and initial characterization of a parametric wing section with aileron and spoiler control surfaces intended for use with the existing facilities at Delft University of Technology. First, the design of the wing and its mechanical and electrical systems is treated. This is followed by a description of the experimental setup and the various tests that were performed. Then the results of the system identification and gust load alleviation tests are shown and discussed.

## **2 DESIGN OF THE WING SECTION**

The design of the wing section is detailed in this section. First, the requirements and constraints are discussed, followed by an overview of the design and layout of the wing section. Then, the design of the mechanical and electrical systems integrated in the wing is presented. Finally, the finalized wing section is presented.

### **2.1 Design requirements and constraints**

As mentioned in the introduction, the new wing section should be designed for use with the existing gust generator and aeroelastic apparatus. The passive wing section already available has a chord of 160 mm, a span of 360 mm and a NACA 0012 profile. Since this wing section has already been proven to work with the aeroelastic apparatus [11], it is chosen as the basis for the new design of the active wing section.

Several requirements were set for the design. To enable research on active control of (non)linear aeroelastic phenomena and the aerodynamic interaction between various control surfaces, the wing section shall be equipped with both aileron and spoiler control surfaces. The wing should be equipped with parametric devices; a free play mechanism in the aileron actuation mechanism and a variable pitch axis location. The former is included to investigate the effect of control surface free play on nonlinear aeroelastic phenomena, while the latter allows stability of the system to be changed and influences the control surface effectiveness. Furthermore, the wing section is required to be a self-contained unit. This requirement is set to keep the hardware architecture simple and to limit the interference of external wiring on the aeroelastic response of the system. Finally, based on the previous requirement, the internal components should be easily accessible.

Based on the requirements, it was determined the wing section should be able to at least fit a single-board computer, instrumentation, two servo actuators, a free play mechanism, mounting structure and a battery/power supply. Looking at commercially available components, the components listed in Table 1 were deemed the best candidates. The choice for these components will be further explained in Section 2.4.

Table 1: List of chosen commercially available components.

Component	Amount	Type
Single-board computer	1	BeagleBone Blue (BBBlue)
Servo actuators	2	BMS-A10V
Battery	2	550 mAh 1S LiPo

## 2.2 General design and layout of the wing section

A CAD model of the wing section was made in CATIA using models of the commercially available components. It was determined that a NACA 0012 airfoil provided insufficient internal space for all the components. In particular, additional clearance was necessary to facilitate the free movement of the servo horns. Therefore it was decided to increase the thickness of the airfoil. As a result, a NACA 0014 airfoil was chosen, providing an additional 3.2 mm of maximum internal height.

Besides the internal components, other drivers for the design are the size and location of the control surfaces. Based on the reviewed literature, common aileron sizes are between  $0.20c$  and  $0.25c$  [2, 12], whereas common sizes for the spoiler range from  $0.10c$  to  $0.15c$  [4, 6, 13], located between  $0.65c$  and  $0.75c$ . To facilitate sufficient space for all the internal components, such as the BBBlue, batteries and the control surface hinge axles and bearings, the choice was made for a  $0.25c$  aileron and a  $0.135c$  spoiler located at  $0.6c$ . An overview of the selected design parameters is given in Table 2. Figure 1 gives an overview of the wing section, including the sign conventions for heave  $h$ , pitch  $\theta$ , aileron deflection  $\beta$ , and spoiler deflection  $\delta$ . Additionally indicated in this figure are the heave and pitch stiffnesses  $K_h$  and  $K_\theta$ .

Table 2: Parameters of the wing section.

Parameter		Value
Airfoil	-	NACA 0014
Chord	$c$	160 mm
Span	$b$	368 mm
Aileron chord	$c_a$	40 mm
Aileron deflection	$\beta$	$\pm 20$ deg
Spoiler chord	$c_s$	21.6 mm
Spoiler deflection	$\delta$	0 deg - 90 deg
Spoiler position	$x_s/c$	0.65

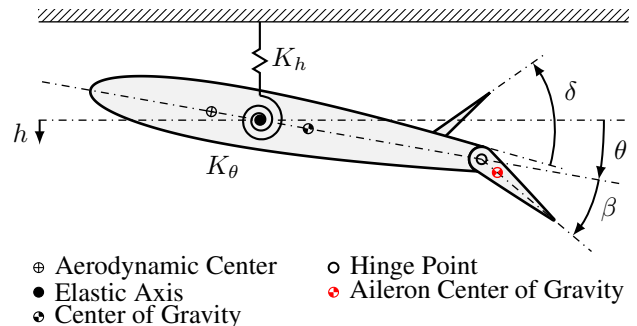


Figure 1: Schematic of the wing section and sign conventions.

With the general dimensions, shape and the majority of the internal components known, the components are positioned in the CAD model. To maintain symmetry in terms of geometry and mass distribution, components were placed symmetrically about the longitudinal axis as much as possible. This is done to limit the effect of such asymmetries on the modal response, and thereby aeroelastic behavior of the wing section. Following the placement of the components, indicated in Figure 2, the internal structure was designed to carry the internal components. This structure consists of two primary components, a set of wooden frames for the main body and control surfaces and an aerodynamic shell.

Figure 2 shows the wooden frames, consisting of chordwise ribs and spanwise spars and longerons. Since the bottom cover is removable, the wooden frames should provide sufficient stiffness to prevent deformation of the wing section under load. Besides determining the outer shape of the

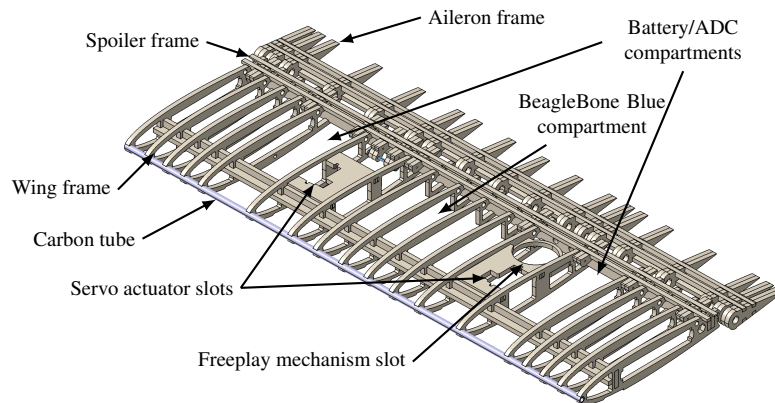


Figure 2: Render of the wing, spoiler and aileron frames.

wing section, the ribs are also modified to accommodate the various internal components. For example, the outer ribs contain a slot for the mounting of the wing section and the middle ribs have a cutout to fit the single-board computer. A carbon fiber tube is glued in the leading edge, providing a smooth, curved surface for the parts of the aerodynamic shell to be glued on to.

The aerodynamic shell, seen in Figure 3, consists of multiple fiberglass components with a thickness of 0.5 mm. As set in the requirements, the internals of the wing section must be easily accessible, therefore the majority of the lower skin consists of a removable cover held in place by magnets for quick access. Additionally, a 3D-printed fairing was used for the aileron pushrod protruding through the bottom cover. With the exception of the bottom cover, all components of the aerodynamic shell are glued to the frames.

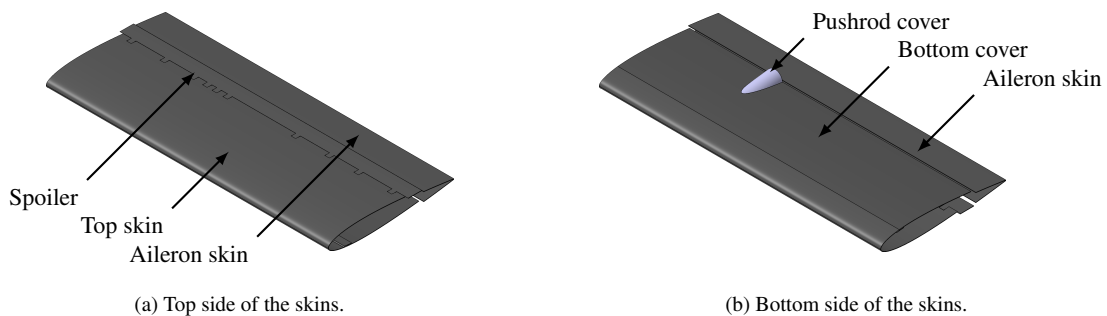


Figure 3: Renders of the wing skins.

### 2.3 Design of the mechanical systems

The mechanical systems of the wing section consist of three distinct separate mechanisms: the first, a conventional three-bar linkage for the spoiler actuation mechanism, with a pushrod connecting the servo horn to the spoiler. The second, the aileron actuation mechanism seen in Figure 4, connects the servo actuator to through two pushrods and free play mechanism (FPM) to the aileron. Finally, the modular mounting mechanism allows for a variable pitch axis location.

The FPM, shown in detail in Figure 5, is included to allow for the effect of control surface free play on aeroelastic phenomena such as flutter, GLA and limit cycle oscillation (LCO) to be quantified. In addition, it can be used to investigate the effects of control surface free play on control laws. The FPM consists of a casing with two independently rotating blocks - an

interchangeable input block and a fixed output block - each connected to the casing by their own ball bearing.

The amount of free play in the system is precisely controlled by the input block. For 0 deg of free play, the contact surfaces of the input block matches that of the output block. Free play is introduced in the mechanism by exchanging the 0 deg input block for one with angled contact surfaces. Up to  $\pm 45$  deg of free play can be implemented with this mechanism, limited by the screws holding the input block in place. In addition to symmetric free play, asymmetric free play is also possible.

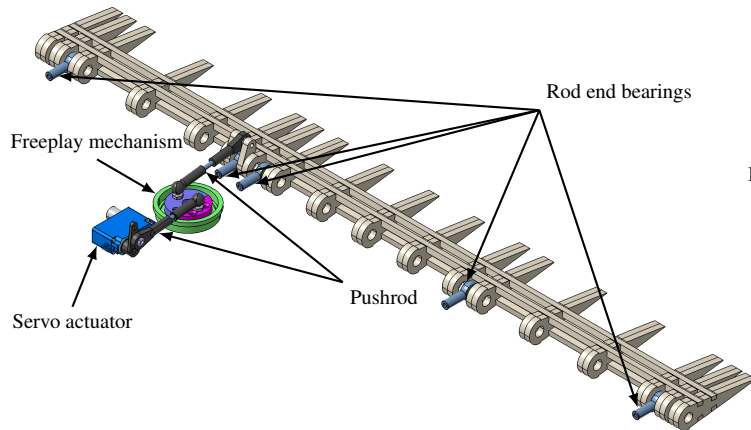


Figure 4: Render of the aileron actuation mechanism.

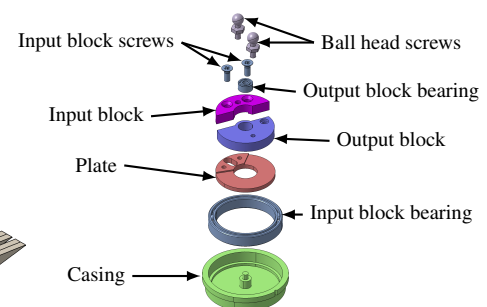


Figure 5: Exploded view of the freeplay mechanism.

The mounting assembly used to suspend the wing in the aeroelastic apparatus, shown in Figure 6, is designed to interface with the existing facilities. The mounting mechanism for the passive wing consists of aluminium ribs at each end of the wing and an axle running throughout the length of the wing [11]. Due to the internal components of the active wing section, a continuous axle was not possible, therefore necessitating the design of a new mounting mechanism.

The developed mechanism consists of an inner rib that has the same outline as the wooden ribs. This rib is glued into the wing section and covered by the aerodynamic shell. A slot machined in this rib allows a pair of mounting plates to be attached to the inner rib. The purpose of the mounting plates is two-fold, first, providing bending stiffness to the wing section and second, enabling the pitch axis location to be adjusted - between  $0.25c$  and  $0.55c$  in  $0.05c$  increments - for the pitch axle. The assembly is capped off with a closing rib on the outside, sitting flush with the aerodynamic shell and covering the mounting plate screws. With exception of the glued inner rib, the modular design of the mounting mechanism allows it to be reused for new, future wing sections.

## 2.4 Design of the electrical system

The electrical system of the wing section consist of a single board computer, the servo actuators connected to the control surfaces, and instrumentation used to measure the aeroservoelastic response of the system.

At the core of the electrical system is the BeagleBone Blue (BBBlue). The BBBlue is a Linux-based, single board computer, designed for robotic applications. This single board computer was chosen to control the wing since it is equipped with a 9-axis inertial measurement unit

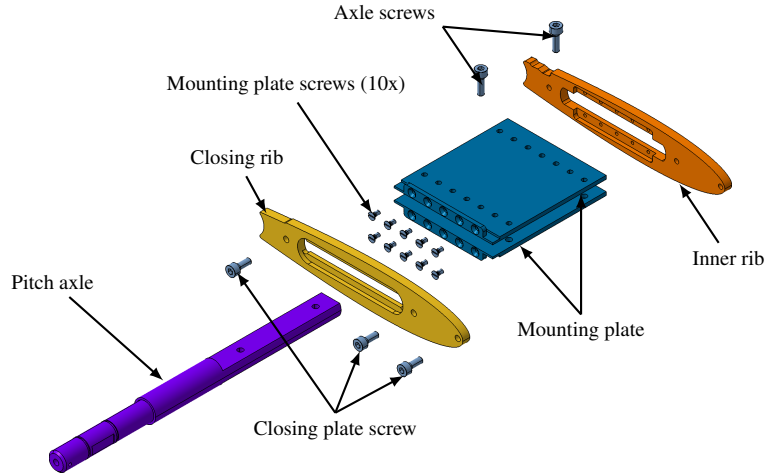


Figure 6: Exploded view of the right-hand side mounting.

(IMU), 8 servo control outputs, 1.8 VDC 12-bit analog-to-digital (ADC), WiFi, and various other input/output connections, all combined in a board with the approximate size of a credit card.

The BBBlue runs on the *Debian 9.5 IoT 2018-10-07* release of the Debian Linux kernel. Using the *Simulink Coder Support Package for BeagleBone Blue Hardware*, the BBBlue is configured to run MATLAB/Simulink models in real-time. The use of Simulink allows for impromptu changes to the control system architecture to be quickly deployed to the BBBlue for testing.

For the control surface actuation, two Blue Bird Model BMS-A10V<sup>a</sup> servo actuators are used. Table 3 provides a comparison of a small selection of commercial off-the-shelf (COTS) servo actuators. Driving parameters for the choice of servo actuators are their size, torque  $T$  and angular speed  $\dot{\delta}_{servo}$  for a given operating voltage  $U$ . In absolute numbers in terms of torque and speed, the Savox SV1232MG performs best, however has three times the mass and volume of the BMS-A10V. Comparing torque to mass and torque to volume ratios, the BMS-A10V outperforms the other servo actuators and was therefore chosen for use in the wing section.

Table 3: Specification comparison of COTS servo actuators at  $U = 6$  VDC.

Type	$L \times W \times H$ [mm]	$m$ [gr]	$T$ [kg cm]	$\dot{\delta}_{servo}$ [s/60 deg]
BBM BMS-A10V	$22 \times 8.0 \times 15.3$	7.4	2.4	0.10
Modelcraft MC-51	$22 \times 9.8 \times 16.2$	6.1	1.3	0.10
Hitec HS-40	$20 \times 8.6 \times 17.0$	4.8	0.8	0.10
Savox SV1232MG	$23 \times 12.0 \times 27.3$	23	4.0	0.06

To provide position feedback, the servo actuators are modified to connect their internal potentiometer to an ADC. As the position signal from the servo actuators exceed the 1.8 VDC limit of the BBBlue ADC, 12-bit ADS1015<sup>b</sup> breakout boards are used to record this signal. These ADCs are connected to the BBBlue using the I2C protocol.

To measure the aeroservoelastic response of the system, the wing section is equipped with several sensors. The BBBlue is equipped with a 9-axis IMU, the MPU9250, which outputs

<sup>a</sup>[https://www.blue-bird-model.com/products\\_detail/74.htm](https://www.blue-bird-model.com/products_detail/74.htm), accessed May 1, 2022.

<sup>b</sup><https://www.adafruit.com/product/1083>, accessed May 1, 2022.

acceleration and magnetic field strength along the x-, y-, and z-axis and angular rates about the aforementioned axes. By enabling an internal algorithm, the IMU can also output the pitch angle estimate based on readings from the gyroscope and magnetometer.

As the IMU output is not noise-free, integration of the acceleration and pitch rate to obtain the heave and pitch degrees of freedom (DOF) introduces drift. To obtain a more accurate measurement for heave and pitch, a linear and rotation variable differential transformer (LVDT/RVDT) are used. The LVDT (Sentech 75DC-500) and RVDT (Midori QP-2HC) measure heave and pitch directly. The variable DC output voltage of these sensors is read by the BBBlue onboard ADC.

The gust generator generates a trigger signal at the start of every gust. This signal is recorded to aid with the synchronizing the data in post-processing. The trigger signal is recorded on one of the GPIO pins of the BBBlue. All input for the BBBlue is summarized in Table 4.

Table 4: Input signals for the BBBlue.

Sensor	Description	Variable	Unit
Potentiometer	Servo angle	$\delta_{servo}$	deg
IMU	acceleration	$\ddot{h}$	m/s <sup>2</sup>
	pitch angle	$\theta$	deg
	pitch rate	$\dot{\theta}$	deg/s
LVDT	heave	$h$	mm
RVDT	pitch angle	$\theta$	deg
GPIO	gust trigger	-	-

The BBBlue requires a 2-cell (2S) LiPo battery to provide sufficient current to drive the servo actuators. However, as mentioned before, it is desirable to distribute the internal components as symmetrically as possible to keep a symmetric mass distribution. The 2S battery was therefore replaced by two single cell (1S), 550 mAh LiPo batteries connected in series. The size and capacity of the batteries were chosen taking into account the airfoil profile and placement of structural components.

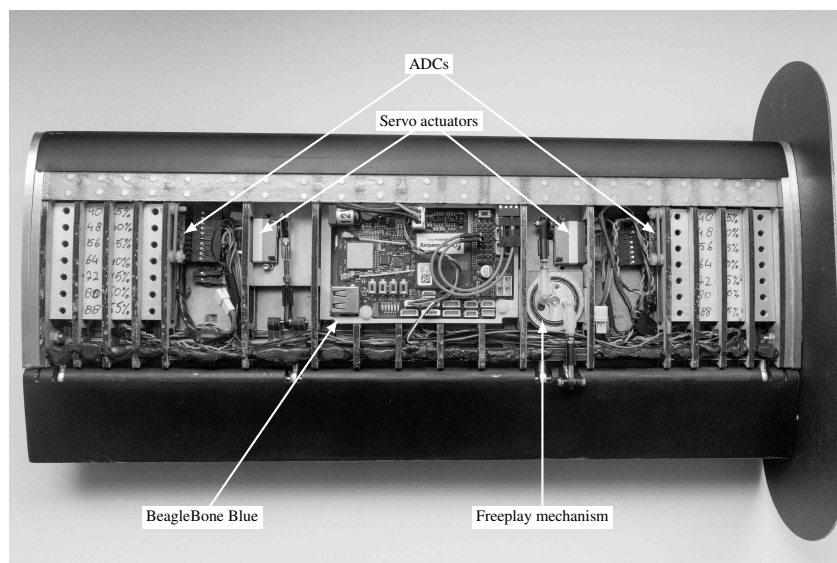


Figure 7: Bottom view of the wing section with the cover and right endplate removed.

## 2.5 Manufactured wing section

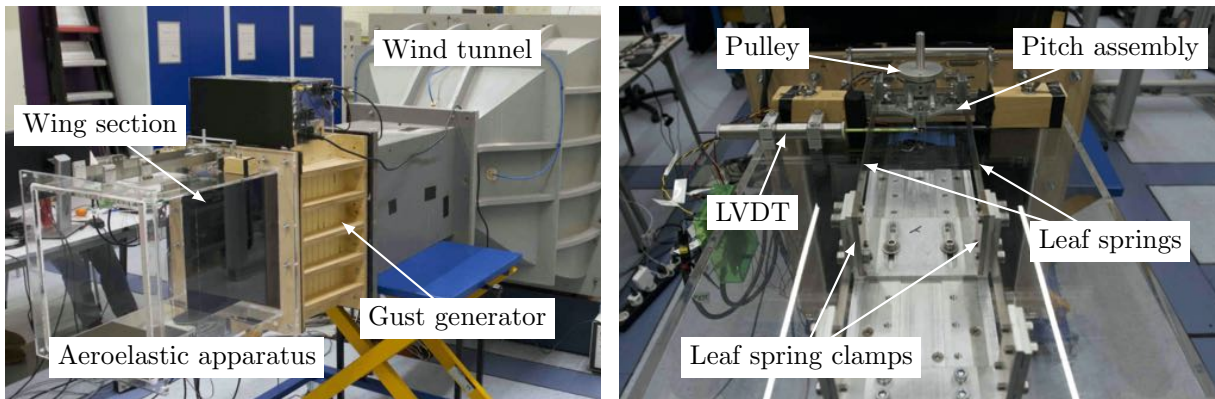
Figure 7 shows the completed and assembled wing section, with the bottom cover removed to show the internal components. Furthermore after the components were finished, various inertial parameters such as mass, mass moment of inertia and center of gravity, were experimentally determined as they present critical input for the numerical model of the wing section. These parameters are summarized in Table 5.

Table 5: Overview of the inertial parameters.

Parameter		Value
Total mass	$m$	531 gr
Aileron mass	$m_a$	58 gr
Spoiler mass	$m_s$	9.7 gr
Wing longitudinal CG	$x_{cg}$	6.09 cm
Wing lateral CG	$y_{cg}$	-0.32 cm
Aileron CG w.r.t. hinge	$x_{cg,a}$	1.34 cm
Spoiler CG w.r.t. hinge	$x_{cg,f}$	0.13 cm
Total MMoI about CG	$I_\theta$	$9.99 \times 10^{-4} \text{ kg m}^2$
Aileron MMoI about hinge axis	$I_\beta$	$1.70 \times 10^{-5} \text{ kg m}^2$
Spoiler MMoI about hinge axis	$I_\delta$	$1.067 \times 10^{-6} \text{ kg m}^2$

## 3 EXPERIMENTAL SETUP

Wind tunnel testing was performed at the M- and W-tunnels at Delft University of Technology. Both are open-circuit blow-down tunnels, with a  $0.4 \text{ m} \times 0.4 \text{ m}$  test section, with low turbulence levels and a maximum attainable speed of  $35 \text{ m/s}^c$ . Attached to the wind tunnel is a gust generator capable of generating sinusoidal and 1-cosine gust excitations with gust frequencies ranging from 0.5 Hz to 12 Hz in 0.5 Hz increments [10]. An overview of the test setup is shown in Figure 8.



(a) Wind tunnel with the gust generator and aeroelastic apparatus.

(b) Top view of the aeroelastic apparatus. Note, the RVDT is placed on the bottom side.

Figure 8: Overview of the test setup.

The wing section itself is mounted in the aeroelastic apparatus developed by Gjerek et al. [11]. The aeroelastic apparatus consists of a rectangular, acrylic section that is mounted to the gust generator and provides heave and pitch DOFs, with adjustable stiffnesses. In addition to the adjustable stiffnesses, weights can be added forward or rearwards of the pitch axis, allowing

<sup>c</sup><https://www.tudelft.nl/lr/organisatie/afdelingen/aerodynamics-wind-energy-flight-performance-and-propulsion/facilities>, accessed on April 27, 2022

both the mass and center of mass of the wing to be easily changed in order to tune the aeroelastic response. The aeroelastic apparatus is designed to closely match the theoretical model of the typical section, a two-dimensional, elastically supported wing section with aileron and heave and pitch DOFs.

The heave DOF is provided by two pairs of cantilever leaf springs, with one end of the springs clamped to the aeroelastic apparatus and the other end connected to a pitch assembly. The axles protruding from both sides of the wing connect to bearings in the pitch assembly. Changing the length of the leaf springs using a pair of movable clamps allows for the spring stiffness in heave to be adjusted. The torsional stiffness on the other hand is provided by a pair of axial springs connected to one of the axles by a pulley. The torsional stiffness can be varied by changing the diameter of the pulley or exchanging the axial springs. The top half of the mechanism is depicted in Figure 8b. More details on the design of the aeroelastic apparatus can be found in [11].

#### 4 METHODOLOGY

This section describes the methodology used during the experimental testing of the wing section. The system identification tests are discussed first, followed by the gust load alleviation experiments.

The first identification test was the ground vibration test (GVT). With the GVT the structural modes of the wing section, along with their corresponding frequencies and damping ratios are identified. The GVT is performed in-situ with the wing section mounted in the aeroelastic apparatus, as an impact test with a roving hammer. The wing is tapped at eight different locations indicated by the blue nodes in Figure 9, using a pair of accelerometers to record the modal response. One accelerometer is placed at the leading edge of the wing section, the other at the opposite side on the trailing edge of the main body as indicated by the red nodes in Figure 9. The obtained results are used during the wind tunnel test to determine the relevant gust frequencies. It is important to note here, that the GVT is performed for the specific configuration of mass, heave and torsional stiffnesses and elastic axis position. For any change in these characteristics, a new GVT must be performed.

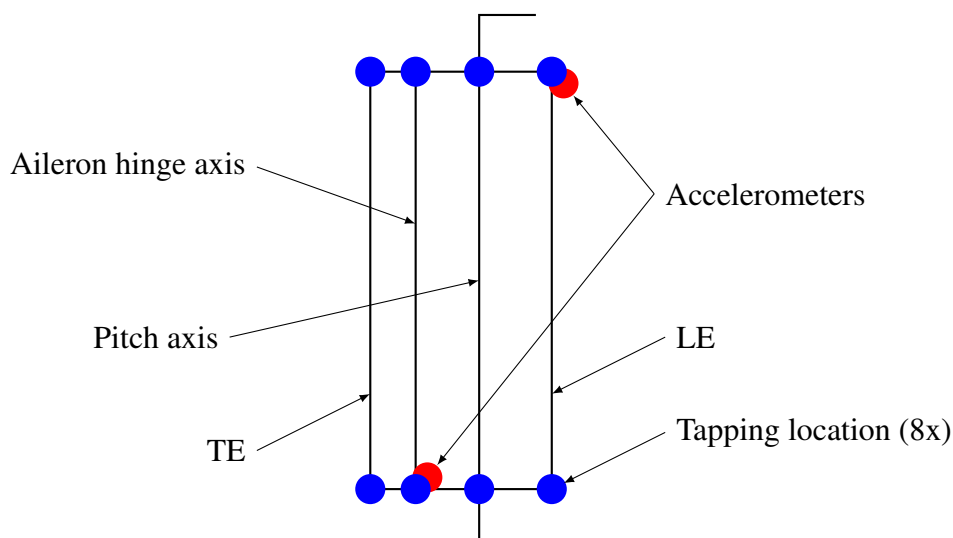


Figure 9: Schematic of the GVT wing model.

Before any of the wind tunnel experiments can be performed, the flutter speed is experimentally

determined in wind on conditions for the current configuration of the aeroelastic apparatus. To find the flutter speed, the parametric flutter margin (PFM) method is applied [14]. With this method, a stabilizing mass is added to the aeroelastic system, and the wing is excited over a range of flow velocities. The system response to the excitations is measured at the stabilizing mass using an accelerometer. With the recorded response, the frequency response function (FRF)  $H$  to the excitation can be determined, which can be expressed in terms of the magnitude frequency response, Eq. (1) and the phase frequency response, Eq. (2). Here,  $M(\omega)$  is the magnitude frequency response expressed in dB and  $\phi(\omega)$  is the phase frequency response expressed in rad.

$$M(\omega) = 20 \log |H(j\omega)| \quad (1) \quad \phi(\omega) = \tan^{-1} (\text{Re}.H(j\omega)/\text{Im}.H(j\omega)) \quad (2)$$

The FRF of the stabilizing mass is recorded over a range of relevant flow velocities. At each measurement point, the gain margin at the phase crossover frequency  $\omega_{pco}$  - the frequency with no phase difference between the system response and its excitation, Eq. (3) - is obtained. The flutter margin FM at each velocity is then given by Eq. (4). The flutter velocity and frequency can then be found by plotting velocity versus the obtained flutter margins and crossover frequencies. The wing section flutters at the velocity where the flutter margin line crosses the 0 dB axis. The flutter frequency  $\omega_f$  corresponds to the interpolated crossover frequency at the flutter velocity  $U_f$ .

$$\phi(\omega_{pco}) = 0 \quad (3) \quad \text{FM} = -M(\omega_{pco}) \quad (4)$$

After determining the flutter speed, the next important point to determine is the control reversal speed. At this speed, the aerodynamic moment due to the aileron deflection creates a pitch deflection that is sufficiently large to reduce the overall angle of attack of a wing, reducing the effect of the aileron deflection or even producing lift in the opposite direction than expected. To determine the control reversal speed, the heave deflection for a certain control surface deflection is measured for increasing air speed, with the pitch DOF free. This speed is relevant for the design of control laws, as it is necessary to switch the sign of the command signal for speeds greater than the control reversal speed to maintain control of the system.

The next set of experiments is performed to obtain frequency response functions for the servo actuators to determine the usable frequency and amplitude range of the servo actuator. The actuator FRFs are obtained by sending a frequency sweep input signal to the servo and measuring the deflection of the servo horn. The experiment is repeated with frequency sweep signals of different amplitudes, to observe the effect of the commanded amplitude on the servo actuator response.

With the next series of test, insight in the aerodynamic interaction between the aileron and spoiler under static conditions is obtained. With the pitch DOF fixed, both control surfaces are swept over their entire deflection range and the heave response is recorded, to be able to determine the static lift considering the heave stiffness. The spoiler deflection  $\delta$  is increased from 0 deg to 90 deg, in 15 deg increments. Smaller, 5 deg increments were used between 15 deg and 30 deg to capture the loss of aileron effectiveness. For each fixed spoiler deflection, the aileron deflection  $\beta$  is swept from  $-20$  deg to 20 deg in 2 deg increments. At each measurement point,

the control surfaces are held steady for 5 s to determine the mean response over the measurement period. This process is repeated for multiple pitch angles to gain insight in the effect of the pitch angle and aileron and spoiler deflections on the aerodynamic response of the wing section.

Finally, a gust load alleviation test was performed as a proof-of-concept, to demonstrate and verify the wing section can accomplish one of the goals for which it is designed. First, the open-loop gust response of the wing section is obtained. For this, the wing is excited with a series of 10 gusts for each of the chosen gust frequency, based on the results from the GVT. From the measured responses, a mean response and standard deviation over time is calculated to determine the repeatability of the response. To show the wing section works as intended, a PID controller is implemented and GLA tests are performed using the aileron and spoiler. The same approach is taken by Schildkamp et al. [15] when conducting active GLA experiments.

## 5 RESULTS AND DISCUSSIONS

The results presented in this section are split up in two parts. In the first part, the results of the various system identification tests are presented. This is followed by the gust load alleviation results in the second part.

### 5.1 System identification tests

First, the GVT results are presented. The first three modes identified during the GVT are the heave, pitch and the rocking mode. Their corresponding frequencies and damping coefficients are summarized in Table 6. The modes are visualized in Figure 10. Due to the design of the aeroelastic apparatus, only the first two modes are considered in this work, as these are the main possible motions for the heave and pitch DOF. With the modes determined, the frequencies for the gust excitation are set below, at, and above the heave and pitch mode, resulting in gust frequencies of 2 Hz, 3.5 Hz, 5 Hz, 6.5 Hz and 7 Hz.

Table 6: Structural modes identified during the GVT.

Mode	Description	Frequency [Hz]	Damping coefficient [-]
1	Heave	3.55	0.072
2	Pitch	6.39	0.099
3	Rocking	11.10	0.037

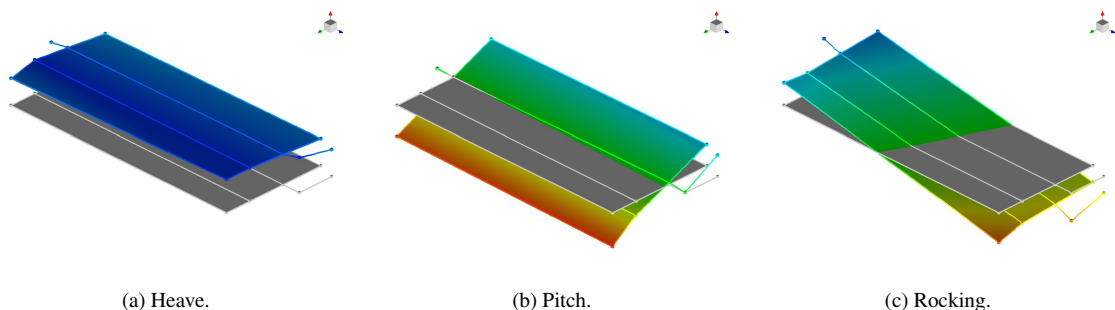
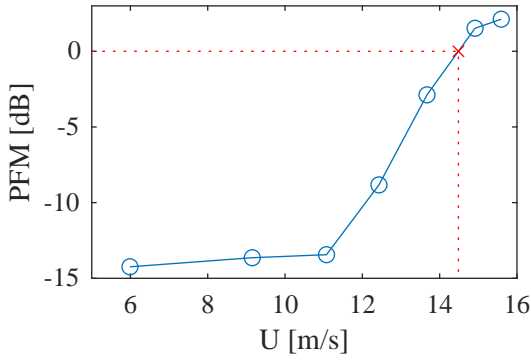


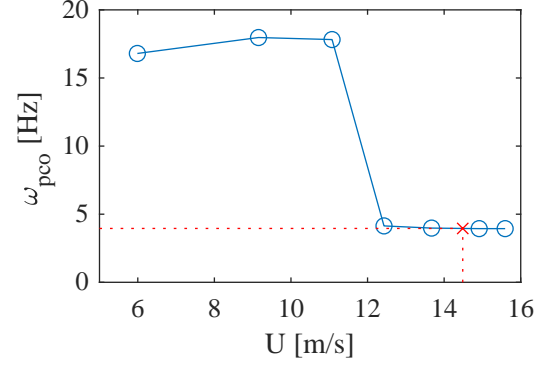
Figure 10: The first three structural modes.

Having completed the GVT and determined the relevant structural modes and gust frequencies, the flutter speed is determined next. The frequency response functions were obtained for flow velocities ranging from 5.6 m/s to 15.8 m/s. The obtained phase crossover frequencies and their corresponding flutter margins are plotted in Figures 11a and 11b. Flutter occurs when

the flutter margin curve in Figure 11a crosses the horizontal axis at 0 dB, giving a flutter speed  $U_f = 14.5$  m/s. The flutter frequency is determined by taking the intersection of the flutter velocity and the frequency curve in Figure 11b, resulting in a flutter frequency  $\omega_f = 3.95$  Hz. Based on the obtained flutter speed, it was decided to perform the remaining wind tunnel tests at 13.6 m/s.



(a) Flutter margin versus velocity. Flutter happens when the flutter margin switches sign from negative to positive at 14.5 m/s.



(b) Flutter frequency versus velocity. At the flutter boundary of 14.5 m/s, the wing section flutters with a frequency of 3.95 Hz.

Figure 11: Parametric flutter margin results.

With the flutter speed known, the next speed to determine is the control reversal speed. As mentioned in Section 4, the heave response to a 20 deg aileron deflection is measured as a function of increasing velocity. As shown in Figure 12. Up to 11.5 m/s an increase in magnitude of  $h$  is observed for increasing speed, as expected. Beyond the velocity of 11.5 m/s however,  $h$  starts to decrease in magnitude, indicating that angle of attack is decreased due to the aerodynamic moment induced by the aileron deflection. Above 14.4 m/s,  $h$  changes sign, indicating control reversal is occurring.

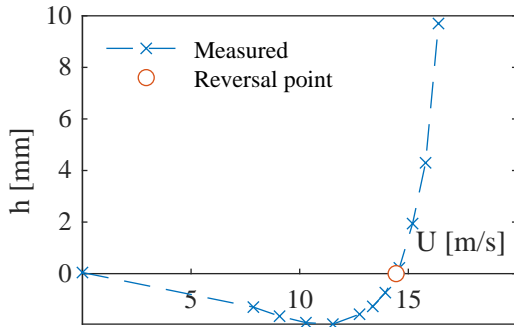


Figure 12: Heave response to a 20 deg aileron deflection versus velocity. Control reversal occurs at  $U = 14.4$  m/s.

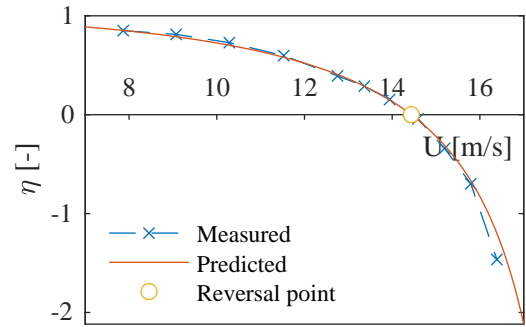


Figure 13: Theoretical and measured control surface efficiency versus velocity.

Figure 13 shows the theoretical and measured control efficiency plotted versus velocity. The control efficiency  $\eta$  is defined by Eq. (5), with  $q$ ,  $q_D$ , and  $q_R$  being the dynamic pressure, the divergence dynamic pressure and control reversal dynamic pressure respectively. Here,  $q_D = 353.6$  Pa and is given by Eq. (6), where the torsional stiffness  $K_\theta = 3.14$  Nm/rad, and a theoretical value of the lift curve slope  $C_{L\alpha} = 2\pi$  rad $^{-1}$  is assumed.

$$\eta = \frac{1 - \frac{q}{q_R}}{1 - \frac{q}{q_D}} \quad (5)$$

$$q_D = \frac{K_\theta}{S(0.5 + a)b C_{L\alpha}} \quad (6)$$

The performance of the servo actuator is assessed next. The commanded and actual position of the servo actuator are shown in Figures 14a and 14b, for amplitudes of 15 deg and 45 deg respectively. The input is the chirp signal with a frequency ranging from 0.1 Hz to 10 Hz. The output is the measured analog signal from the servo actuator potentiometer, converted to deflection angle.

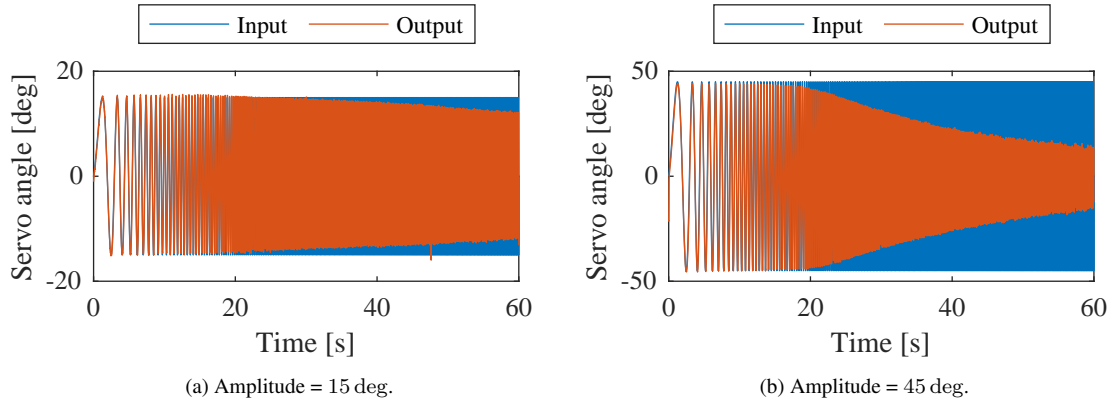


Figure 14: Servo response to a chirp signal from 0.1 Hz to 10 Hz.

As expected, Figure 14 shows the decline in actuator performance for increasing commanded amplitude and saturation at higher frequencies. The same data, converted to the frequency domain, is shown in Figure 15. The Bode plot shows a near constant magnitude response for the 15 deg amplitude, and its cutoff frequency lies outside of the tested frequency range. At 10 Hz, a magnitude reduction of  $-2$  dB is obtained, corresponding to 80% of the commanded angle at  $t = 60$  s in Figure 14a. The phase response lags over the entire frequency range, with the increase in lag worsening from  $-25$  deg at 3 Hz to  $-75$  deg at 10 Hz.

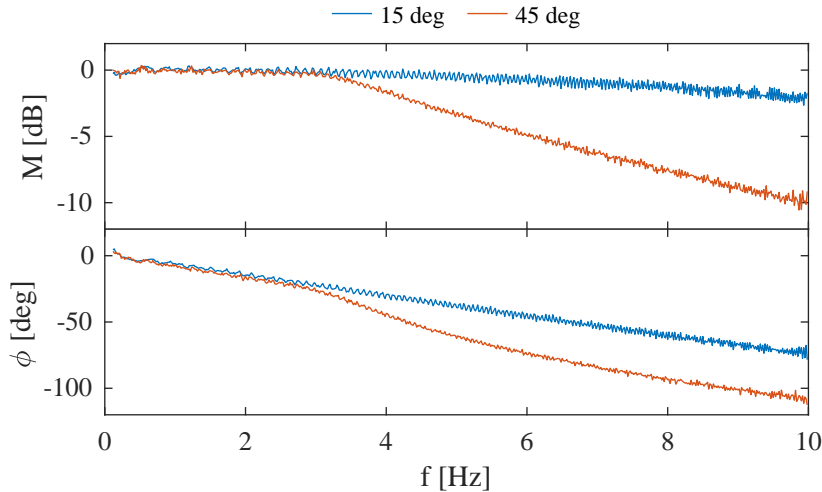


Figure 15: Bode plot of the servo actuator response.

For the 45 deg amplitude, the magnitude is constant up until 3 Hz, after which the magnitude starts to decline rapidly. The magnitude response has a cutoff frequency of 7 Hz, when a 6 dB reduction in magnitude is measured. At 10 Hz a magnitude reduction of  $-10$  dB is achieved, also corresponding to Figure 14b, where only 30% of the commanded magnitude is achieved. The phase response is similar to the 15 deg response until 3 Hz. After this point, the phase lag increases more sharply compared to the 15 deg case, to approximately  $-105$  deg at 10 Hz. It is

shown that the performance envelope of the actuation mechanism depends on the commanded amplitude of the servo actuator.

The static aerodynamic response of the wing section for varying static control surface deflections is shown in Figure 16 for fixed pitch angles of 0 deg, 15 deg and  $-15$  deg, the average standard deviation for each of these curves is given in Table 7.

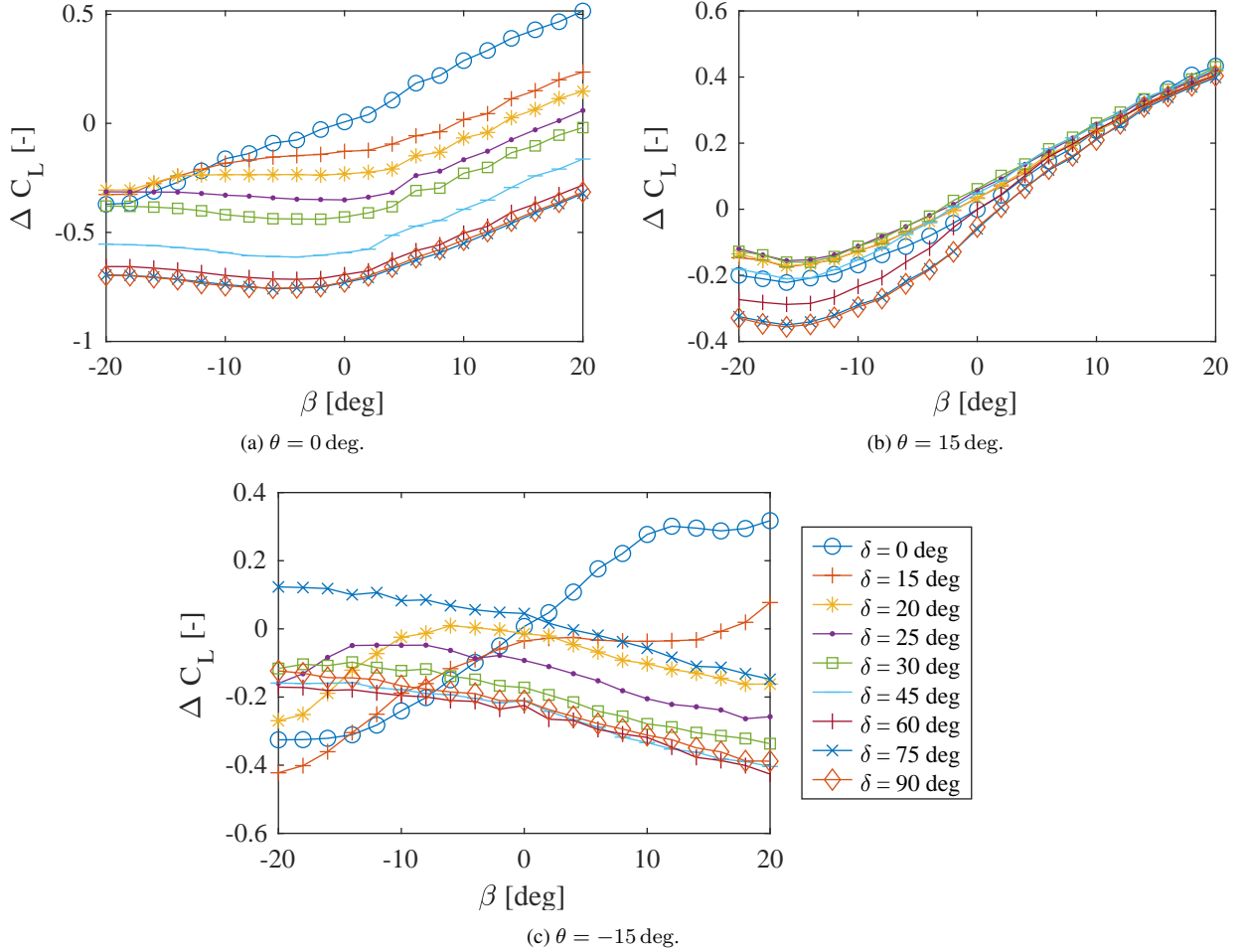


Figure 16:  $\Delta C_L - \beta$  curves for varying  $\delta$ ,  $Re = 1.245 \times 10^5$ .

Considering the case of  $\theta = 0$  deg first, the aerodynamic responses in Figure 16a can be split in two. The linear curves for  $\beta > 0$  deg show the aerodynamics are dominated by the aileron, with an offset between the different curves due to a decrement in lift caused by the spoiler. For  $\beta < 0$  deg, the spoiler dominates the aerodynamic response, as is evident from the nonlinear behavior. For these specific cases, the aileron operates in the turbulent wake of the spoiler.

For the case of  $\delta = 0$  deg, the  $\Delta C_L - \beta$  curve shows a nearly linear response due to the aileron deflection, as can be expected according to linear aerodynamic theory. For spoiler deflections between 15 deg and 25 deg, several interesting phenomena can be observed where the aerodynamics are dominated by the deflection of the spoiler. First, due to the interaction of the aileron and spoiler, the negative lift increment is reduced at  $\beta = -20$  deg. Secondly, a reduction in the lift curve slope is visible for  $-10$  deg  $\leq \beta \leq 0$  deg at  $\delta = 15$  deg, indicating a decrease in aileron effectiveness. Increasing the spoiler deflection to 20 deg, a loss of aileron effectiveness can be observed, as indicated by the zero slope of the  $\Delta C_L - \beta$  curve. Further increasing the deflection of the spoiler leads to aerodynamic reversal of the aileron, having a negative slope

for increasing aileron deflection. Increasing the spoiler beyond 60 deg has little effect on  $\Delta C_L$ , with only a 5% difference between  $\delta = 60$  deg and  $\delta = 90$  deg, this difference is negligible.

For the next case,  $\theta = 15$  deg, which corresponds to positive angle of attack of 15 deg, the  $\Delta C_L - \beta$  curves are shown in Figure 16b. Contrary to the case for  $\theta = 0$  deg, all these curves show the same general trend. Aerodynamic reversal of the aileron occurs again for  $-20 \text{ deg} \leq \beta \leq -16 \text{ deg}$ , after which the response increases quasilinearly for increasing aileron deflection. Again, the aerodynamic response for  $\beta > 0$  deg is dominated by the aileron and the influence of the spoiler seems negligible as  $\beta$  goes to 20 deg, as  $\Delta C_L$  converges to the same value for all spoiler deflections. The difference between the curves for  $\delta = 75$  deg and  $\delta = 90$  deg is again negligible.

The final case is the set of  $\Delta C_L - \beta$  curves for  $\theta = -15$  deg, shown in Figure 16c. Immediately visible in Table 7 is the increase in standard deviation by an order of magnitude for  $\delta > 15$  deg compared to the responses for  $\theta = 0$  deg and  $\theta = 15$  deg. The hypothesis for this increase is that flow separation occurs on both sides of the airfoil, at the leading edge of the bottom surface and at the trailing edge of the spoiler on the top surface. Loss of control surface effectiveness can be observed at  $\delta = 15$  deg between  $\beta = 4$  deg and 14 deg. Additionally, aerodynamic reversal is again visible in all curves except  $\delta = 0$  deg. For spoiler deflections greater than 25 deg, the entire response experiences aerodynamic reversal. The case for  $\delta = 75$  deg follows the same general trend as the other cases with spoiler deflections greater than 25 deg, however this case is offset by approximately 0.25. The experiment was repeated two additional times for this particular case, yielding the same result.

Table 7: Average standard deviation of the  $\Delta C_L - \beta$  curves for varying pitch angles.

$\theta$ [deg]	$\beta$ [deg]								
	0	15	20	25	30	45	60	75	90
-15	0.0097	0.0097	0.0743	0.0817	0.0820	0.0825	0.0904	0.1069	0.1112
0	0.0088	0.0133	0.0104	0.0098	0.0102	0.0096	0.0084	0.0083	0.0085
15	0.0298	0.0332	0.0339	0.0323	0.0298	0.0201	0.0152	0.0136	0.0153

## 5.2 Gust load alleviation

In this final part, results for GLA are presented. The open-loop gust responses were obtained at gust frequencies of 2 Hz, 3.5 Hz, 5 Hz, 6.5 Hz and 7 Hz at a flow velocity  $U = 13.6$  m/s. These values give a reduced frequency  $k$  ranging from 0.07, quasi-steady flow, to 0.26, highly unsteady flow. The theoretical gust profiles are shown in Figure 17.

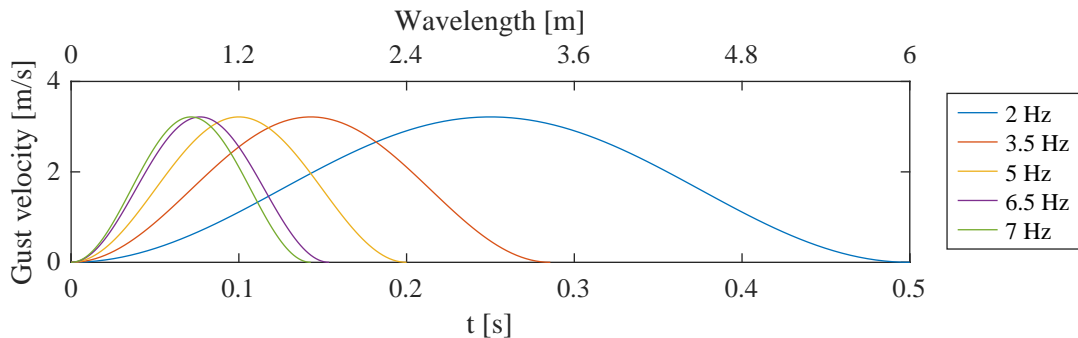


Figure 17: Gust profiles for gust frequencies of 2 Hz, 3.5 Hz, 5 Hz, 6.5 Hz, and 7 Hz at  $U = 13.6$  m/s.

The open-loop response in heave is shown in Figure 18. The maximum amplitude and damping

coefficient as a function of gust frequency are shown in Figure 19. The damped harmonic heave motion shows the open-loop system is stable, albeit highly underdamped, with a damping coefficient close to zero. Furthermore, the first half period of the transient response closely follows the shape of the gust profiles, whereas the remaining part of the transient response is dominated by the first heave mode, oscillating with a frequency of approximately 3.5 Hz.

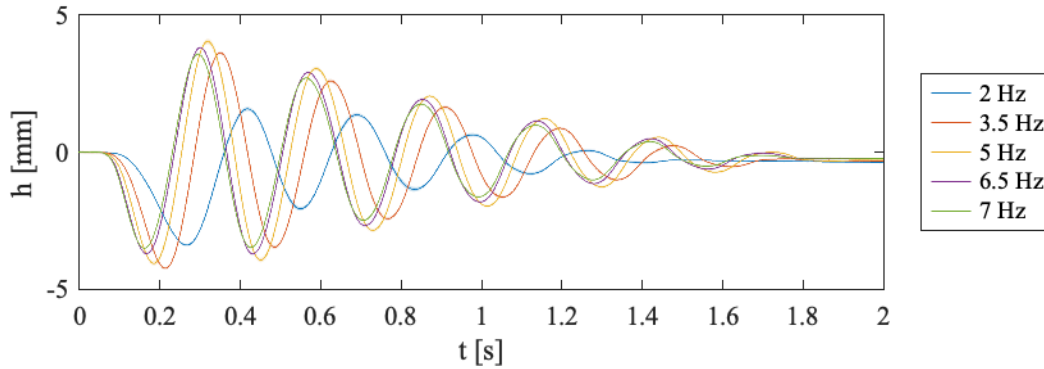


Figure 18: The open-loop heave response for increasing gust frequencies.

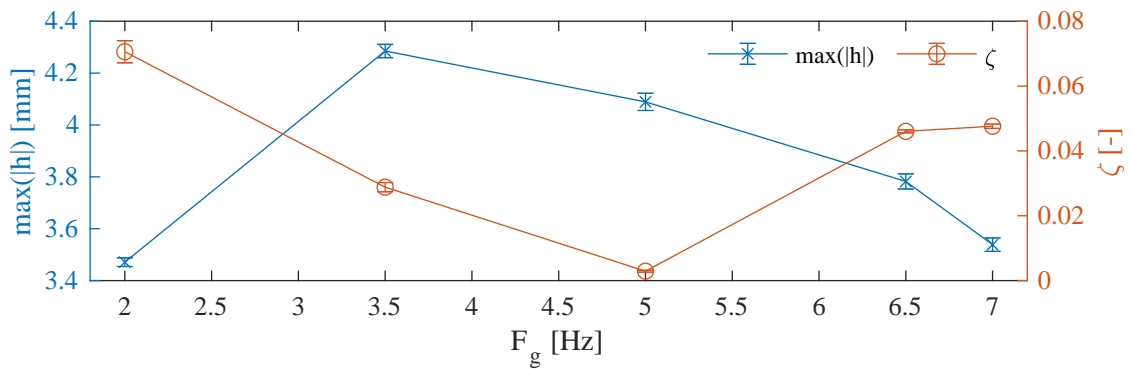


Figure 19: Comparison of the open-loop maximum amplitude and damping coefficient versus gust frequency.

After obtaining the open-loop gust responses, the experiment was repeated, with a PID control system enabled, to obtain the closed-loop response. The control system consists of a manually tuned PID controller using the heave acceleration  $\ddot{h}$  as input. It should be noted here, that the intention of these results is a proof-of-concept of the functionality of the active wing section and its subsystems. As such these results do not reflect optimal results for GLA.

Figure 20 shows a comparison of the open-loop and the closed-loop gust response using aileron and spoiler for a gust frequency of 3.5 Hz. For aileron control a proportional gain  $K_P = 5$  was used, for the spoiler  $K_P = 20$ . Comparing the open-loop with the closed-loop aileron response, only a slight increase in damping is achieved, with a negligible decrease in peak displacement.

The closed-loop spoiler response however shows a different picture. Damping is greatly increased (13x) compared to the open-loop response, the peak amplitude is reduced by 48% and the RMS amplitude is reduced by 63%. While these results show great improvement over the open-loop response, an increase in standard deviation is also observed. This is attributed to the nature of spoiler aerodynamics as ailerons effectively change the camber of an airfoil, where the flow remains attached for low to moderate deflection angles. Spoilers on the other hand, operate by creating flow separation, producing turbulent wakes and leading to an increased stochastic

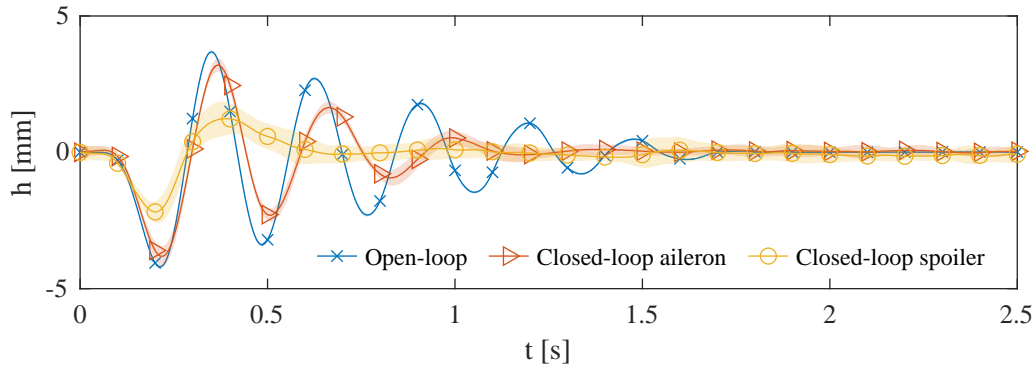


Figure 20: Comparison of the open-loop and closed-loop gust responses.

response.

## 6 CONCLUSION

This paper presents the development and initial testing of an active, parametric wing section. The wing section is equipped with a  $0.25c$  aileron and  $0.135c$  spoiler located at  $0.60c$  and is intended for future research on the control of aeroelastic phenomena. The wing section is completely self-contained, with the power supply, instrumentation and a single-board computer integrated into it. Inclusion of a freeplay mechanism in aileron actuation mechanism allows for the investigation of the effect of control surface free-play on aeroelastic phenomena.

Various system identification tests have been performed on the model. A ground vibration test was performed identifying the dominant structural modes of the aeroelastic apparatus. The control reversal speed and flutter speed were determined using wind tunnel testing. The frequency response of the servo actuator was obtained to gain insight in its performance. As expected, a degradation in both amplitude and phase performance is seen for higher frequencies and higher commanded amplitudes.

Static aerodynamic responses show a clear distinction in which control surface dominates the flow. A loss of aileron effectiveness is observed for zero pitch angle and a  $20^\circ$  spoiler deflection. Furthermore aerodynamic reversal of the aileron is seen for spoiler deflection cases at zero and negative pitch angles. The outliers and large spread in data for the combination of negative pitch angle and spoiler deflection requires further investigation.

As a proof-of-concept, initial open- and closed-loop GLA tests were performed using a PID control with both aileron and spoiler. Open-loop tests showed a largest peak amplitude for a gust frequency of  $3.5\text{ Hz}$ , near the natural frequency of the first mode in heave. Closed-loop tests show that the system can effectively detect and respond to gust excitations, achieving the purpose for which the wing section was designed and built.

## 7 OUTLOOK

Initial tests using the developed platform show promising results. The current setup allows for the quick deployment of changes in the control algorithms, enabling a fast turnaround time during wind tunnel testing. The wing section has already been used for research on an incremental nonlinear dynamic inversion (INDI) controller for load alleviation and flutter suppression using the aileron [15]. This research will be further expanded to using the spoiler with the INDI

controller and implementing MIMO control to control the heave and pitch response using the aileron and spoiler.

Various system characteristics such as the structural modes, flutter and reversal speed, are only valid for the tested configuration and therefore need to be identified first when performing tests using different pitch axis location, mass distribution and heave and pitch stiffnesses. Characterization of the servo actuator has now only been performed without external loads. As the application of external loads is likely to degrade the actuator response further, this necessitates thorough testing of servo actuator to fully characterize its performance as a function of commanded frequency and amplitude and external load. The static aerodynamic responses have been obtained for pitch angles of 0 deg, 15 deg and  $-15$  deg. To further develop an experimental aerodynamic model for the wing section, these responses will also need to be obtained for intermediate pitch angles. This experimental aerodynamic model can in turn be used to develop numerical models of the wing section. Additionally, anomalous behavior observed with the aerodynamic response for  $\theta = -15$  deg will be investigated using CFD.

Though the current setup is working, various improvements are still envisioned. The most important change is replacing the LiPo batteries with a power supply. Even though the batteries were originally planned to be in the wing section, the capacity of the batteries is too small for testing in practice, requiring a change of batteries every hour, significantly impeding the rate of testing. Additionally, whenever a battery must be changed the wing section must be tempered with, which can potentially introduce measurement uncertainties. Another important aspect is the degradation in servo actuator performance in both terms of speed and torque due to the decline in electric potential during discharging.

A second improvement is the addition of magnetic rotary position sensors (AS5600<sup>d</sup>) on the aileron and free play mechanism and the spoiler. These sensors will serve several purposes. First, the actual deflections of the control surfaces can be measured directly. Especially for the aileron, this is a crucial feature when free play is introduced. Second, with the measured deflection of both actuators and control surfaces, the flexibility in the actuation mechanisms can be assessed. As the sensors operate using a magnetic field, no additional friction is introduced in the mechanisms.

## 8 REFERENCES

- [1] Livne, E. (2018). Aircraft active flutter suppression: State of the art and technology maturation needs. *Journal of Aircraft*, 55(1), 410–450. ISSN 15333868. doi: 10.2514/1.C034442.
- [2] Viperman, J. S., Clark, R. L., Conner, M., et al. (1998). Experimental Active Control of a Typical Section Using a Trailing-Edge Flap. *Journal of Aircraft*, 35(2), 224–229. ISSN 0021-8669. doi:10.2514/2.2312.
- [3] Barzgaran, B., Quenzer, J. D., Zongolowicz, A., et al. (2019). Low-cost wind tunnel studies of gust alleviation control techniques. In *International Forum on Aeroelasticity and Structural Dynamics 2019, IFASD 2019*, June. Savannah, GA, pp. 1–18.
- [4] Cassaro, M., Nagy, A., Marzocca, P., et al. (2014). Novel Active Control Strategy for LCO and Flutter Suppression by a Coordinated Use of Multiple Distributed Surface Actuators.

---

<sup>d</sup><https://ams.com/en/as5600>, accessed May 15, 2022.

- In *Volume 1: Advances in Aerospace Technology*, vol. 1. American Society of Mechanical Engineers. ISBN 978-0-7918-4642-1, p. 7. doi:10.1115/IMECE2014-36905.
- [5] Cassaro, M., Battipede, M., Marzocca, P., et al. (2015). Aeroelastic System Control by a Multiple Spoiler Actuation and MRAC Scheme. In *56th AIAA/ASCE/AHS/ASC Structures, Structural Dynamics, and Materials Conference*, January. Reston, VA: AIAA. ISBN 978-1-62410-342-1, pp. 1–14. doi:10.2514/6.2015-1851.
- [6] Lancelot, P. and De Breuker, R. (2016). Passively actuated spoiler for gust load alleviation. *27th International Conference on Adaptive Structures and Technologies*.
- [7] Bonnema, K. L. and Smith, S. B. (1988). AFTI/F-111 Mission Adaptive Wing flight research program. In *4th Flight Test Conference*. Reston, VA: American Institute of Aeronautics and Astronautics, pp. 155–161. doi:10.2514/6.1988-2118.
- [8] Wang, X., Mkhoyan, T., Mkhoyan, I., et al. (2021). Seamless active morphing wing simultaneous gust and maneuver load alleviation. *Journal of Guidance, Control, and Dynamics*, 44(9), 1649–1662. ISSN 15333884. doi:10.2514/1.G005870.
- [9] Córcoles, X. C., Mertens, C., Sciacchitano, A., et al. (2022). Wing Stiffness and Hinge Release Threshold Effects on Folding Wingtip Gust Load Alleviation. *AIAA Science and Technology Forum and Exposition, AIAA SciTech Forum 2022*, 1–29. doi:10.2514/6.2022-1559.
- [10] Geertsen, J. A. (2020). *Development of a Gust Generator for a Low Speed Wind Tunnel*. Master's thesis, ETH Zürich.
- [11] Gjerek, B., Drazumeric, R., and Kosel, F. (2014). A Novel Experimental Setup for Multi-parameter Aeroelastic Wind Tunnel Tests. *Experimental Techniques*, 38(6), 30–43. ISSN 07328818. doi:10.1111/j.1747-1567.2012.00839.x.
- [12] Layton, J. B. (1995). Aeroservoelastic tailoring for gust response of a typical section aeroelastic model. In *Collection of Technical Papers - AIAA/ASME/ASCE/AHS/ASC Structures, Structural Dynamics and Materials Conference*, vol. 1. ISSN 02734508, pp. 306–313. doi:10.2514/6.1995-1192.
- [13] Dempster, J. B. and Roger, K. L. (1966). Evaluation of B-52 structural response to random turbulence with various stability augmentation systems. In *3rd Annual Meeting*. Reston, VA: American Institute of Aeronautics and Astronautics, p. 14. doi:10.2514/6.1966-998.
- [14] Sodja, J., Roizner, F., De Breuker, R., et al. (2018). Experimental characterisation of flutter and divergence of 2D wing section with stabilised response. *Aerospace Science and Technology*, 78, 542–552. ISSN 12709638. doi:10.1016/j.ast.2018.05.014.
- [15] Schildkamp, R., Chang, J., Sodja, J., et al. (2022). Incremental Nonlinear Control For Aeroelastic Wing Load Alleviation and Flutter Suppression. In *International Forum on Aeroelasticity and Structural Dynamics 2022, IFASD 2022*, June. Madrid.